

Supporting Online Material

"Dimensionality Control of Electronic Phase Transitions in Nickel-Oxide Superlattices"

A. V. Boris^{1,*}, Y. Matiks¹, E. Benckiser¹, A. Frano¹, P. Popovich¹, V. Hinkov¹,
P. Wochner², M. Castro-Colin², E. Detemple², V. K. Malik³, C. Bernhard³,
T. Prokscha⁴, A. Suter⁴, Z. Salman⁴, E. Morenzoni⁴,
G. Cristiani¹, H.-U. Habermeier¹, and B. Keimer^{1,*}

¹ Max-Planck-Institut für Festkörperforschung,
Heisenbergstrasse 1, D-70569 Stuttgart, Germany

² Max-Planck-Institut für Metallforschung,
Heisenbergstrasse 3, D-70569 Stuttgart, Germany

³ Department of Physics, University of Fribourg and
Fribourg Center for Nano Materials, CH-1700 Fribourg, Switzerland

⁴ Laboratory for Muon Spin Spectroscopy,
Paul Scherrer Institute, CH-5232 Villigen PSI, Switzerland

To whom correspondence should be addressed:

E-mail: *A.Boris@fkf.mpg.de,* B.Keimer@fkf.mpg.de.

Methods and materials

Sample preparation and characterization

High-quality superlattices (SLs) composed of N u.c. thick consecutive layers of LaNiO_3 and LaAlO_3 were grown by pulsed-laser deposition from stoichiometric targets using a KrF excimer laser with 2 Hz pulse rate and 1.6 J/cm^2 energy density. Both compounds were deposited in 0.5 mbar oxygen atmosphere at 730°C and subsequently annealed in 1 bar oxygen atmosphere at 690°C for 30 min. We have grown SLs on two kinds of single-crystalline substrates: SrTiO_3 ,

Table SI: Average lattice constants of 100 nm thick $N = 2$ SLs grown on (001)-oriented SrTiO₃ and LaSrAlO₄ substrates (determined from the main (103) layer Bragg peak positions in Figs. 1B and 1C) in comparison with the lattice constants of strain-free pseudo-cubic LaNiO₃ and LaAlO₃ and the same substrates.

	SL on LaSrAlO ₄	SL on SrTiO ₃	LaNiO ₃	LaAlO ₃	LaSrAlO ₄	SrTiO ₃
a, b (Å)	3.769	3.845	3.837	3.789	3.756	3.905
c (Å)	3.853	3.790	3.837	3.789	12.636	3.905

which induces tensile strain in the overlayer, and LaSrAlO₄, which induces compressive strain (see Table SI). All substrates were 10 mm×10 mm×0.5 mm or 5 mm×5 mm×0.5 mm (001)-oriented plates with a miscut angle $< 0.1^\circ$. We chose to work on 100 nm thick SLs in order to enhance the dielectric response and to confine the muon stopping distribution within the SL. The chosen thickness range also allows us to avoid complications arising from initial growth of TMO layers on a substrate (S1). The growth rates for the individual layers were controlled by counting laser pulses in combination with feedback from high-resolution x-ray diffraction measurements. The crystallinity, superlattice structure, and sharpness of the interfaces (with roughness < 1 u.c.) were verified by momentum-dependent x-ray reflectivity and high-resolution hard x-ray diffraction scans which revealed, besides the perovskite Bragg reflections, satellite peaks due to the long-range multilayer superstructure and Kiessig fringes caused by total-thickness interference.

Representative scans along the specular truncation rod are shown in Fig. S1 for samples grown on the different substrates with different individual layer thicknesses N (u.c.), and total thicknesses D (Å). Symmetrically around the (001) layer Bragg peak one can see superlattice satellites and $M - 2$ thickness fringe maxima, where M is the number of bilayer repetitions. The position of the satellites corresponds to a LaNiO₃ (N u.c.)|LaAlO₃ (N u.c.) bilayer thickness of 30 ± 1 Å and 15.5 ± 0.5 Å for the $N = 4$ (Figs. S1A and S1B) and $N = 2$ (Figs. 1C and 1D), respectively, that is in a good agreement with the $2Nc$ value, where c is the average epilayer lattice constant in Table SI. Accordingly, the Kiessig fringes in Figs. S1 and S2 correspond to the total thickness $M \times 2Nc$. The thickness fringes for the 100 nm thick $N = 2$

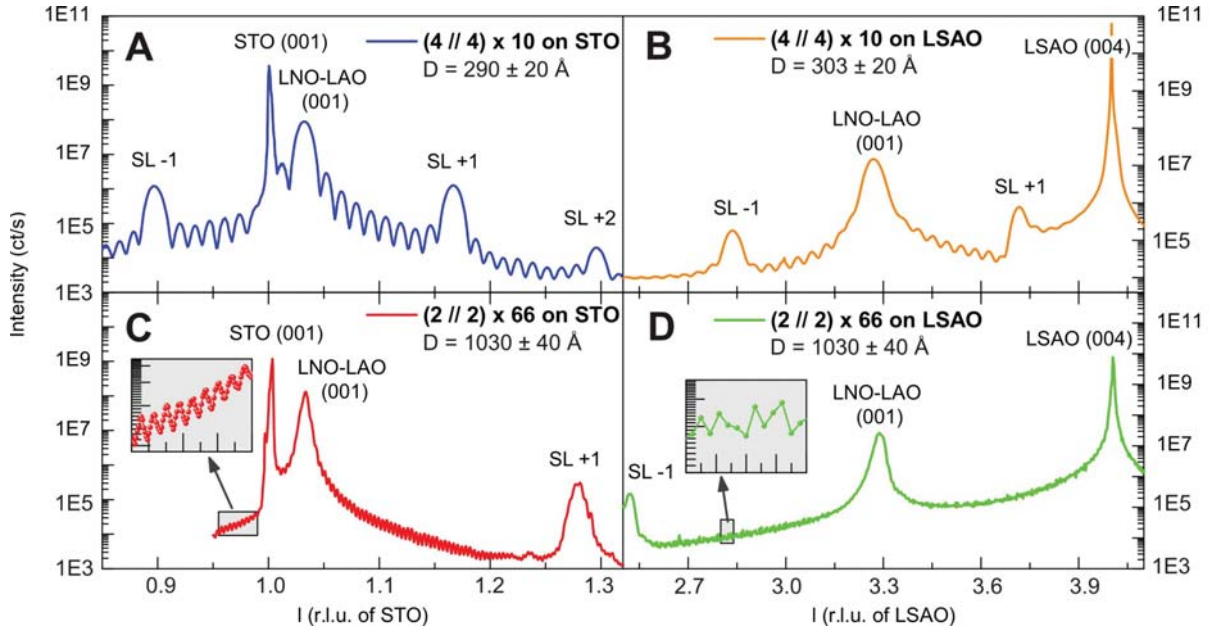


Figure S1: High-resolution x-ray diffraction measured with 10 keV synchrotron radiation at the MPI-MF beamline of the ANKA facility at the Karlsruhe Institute of Technology for the (A, B) 30 nm ($N = 4$) and (C, D) 100 nm ($N = 2$) thick superlattices on (A,C) SrTiO₃ and (B, D) LaSrAlO₄. The thickness of the SL in (D) is determined from the hard x-ray reflectivity measurements in Fig. 2D. The 100 nm thick samples were used for low-energy muon spin rotation and ellipsometry experiments.

SL on LaSrAlO₄ are damped at higher l values in Fig. S1D, but well resolved in Fig. S2D. The x-ray reflectivity shown in Fig. S2 was also used to characterize the superlattice structure and sharpness of the interfaces. From fits to the reflectivity, using the Parratt algorithm and tabulated values for the optical constants (S_2, S_3, S_4), we obtained the thickness (d_{LAO}, d_{LNO}) and roughness ($\sigma_{LAO}, \sigma_{LNO}$) of the individual layers. Using a minimal set of fitting parameters (assuming M identical LaNiO₃ and LaAlO₃ layers), we show in Fig. S2 a good description of the data. The roughness parameters are all around 1 u.c or less and represent values averaged over a large area of $\sim(10 \times 1)$ mm which corresponds to the x-ray spot size and inevitably contains planar defects such as stacking faults. This indicates the presence of atomically flat and abrupt interfaces. Some of the samples were also checked by high-resolution transmission electron microscopy (TEM), providing a local picture of the atomic stacking sequence. In Fig.

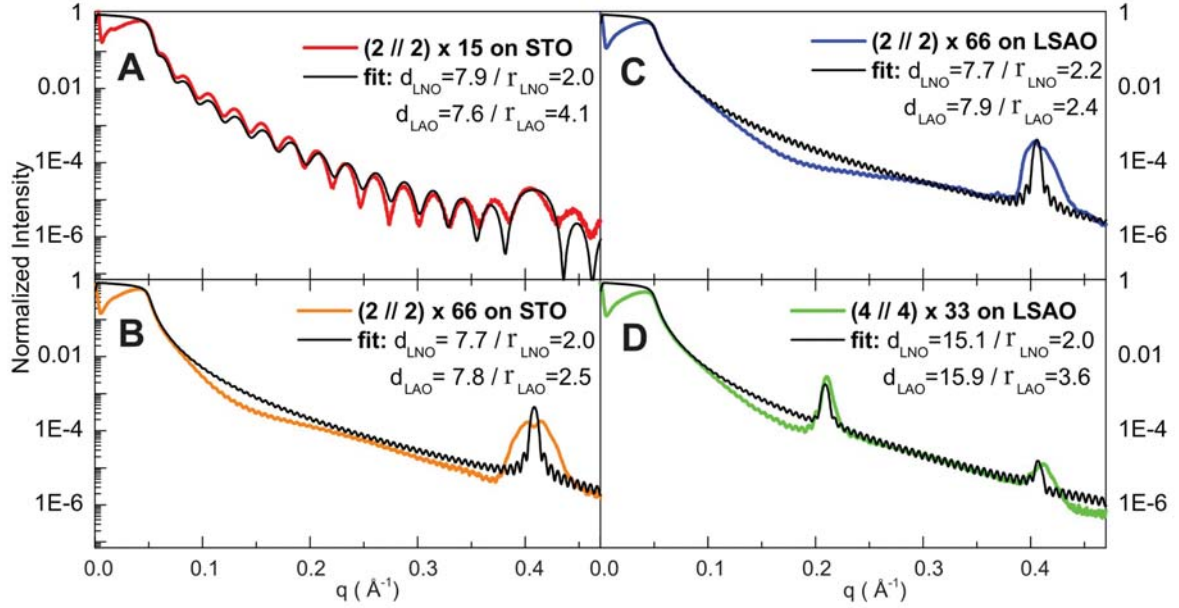


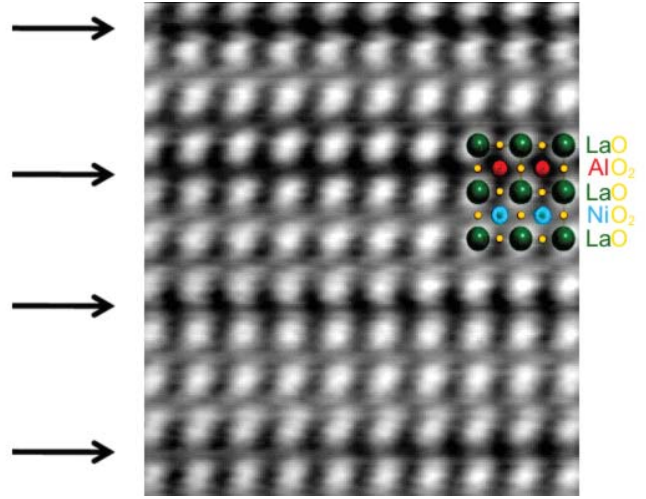
Figure S2: Hard x-ray reflectivity measured with Cu $K\alpha$ radiation and fits for the (A) 23 nm and (B) 100 nm thick $N = 2$ superlattices on SrTiO₃ and 100 nm thick (C) $N = 2$ and (D) $N = 4$ superlattices on LaSrAlO₄. The samples in (C-D) were used for low-energy muon spin rotation and ellipsometry experiments.

S3 a high-angle annular dark-field image of a LaNiO₃ (2 u.c.)|LaAlO₃ (1 u.c.) SL is shown. In this imaging mode, also known as Z -contrast, the contrast is proportional to Z^n , where Z is the atomic number and n is about 1.7. Subsequent dark (marked by arrows) and bright layers show a chemical variation of the layer system. In this example a sequence of two LaNiO₃ layers and one LaAlO₃ layer is visible which shows that even single layers can be deposited without distinct intermixing. The superior quality of our samples is also supported by resonant reflectivity measurements performed on a sample grown under the same conditions. The analysis of those data allowed some of us to determine the atomic-layer resolved orbital polarization in these superlattices (S5).

Substrate-induced strain and relaxation effects

In general, the physical properties of thin films are strongly influenced by substrate-induced

Figure S3: High-angle annular dark field image of the LaNiO_3 (2 u.c.)| LaAlO_3 (1 u.c.) superlattice. Subsequent dark (marked by arrows) and bright layers show the chemical variation of the layer system.



strain and relaxation effects. It has thus far proven difficult to separate the influence of the dimensionality from that of other parameters such as the strain-induced local structural distortions and interfacial defects. In order to discriminate between these effects we chose to work on SLs grown on both SrTiO_3 , which induces tensile strain in the overlayer, and LaSrAlO_4 , which induces compressive strain. Our comprehensive reciprocal-space mapping (RSM) measurements (S6) supplemented by high-resolution TEM micrographs verified that strain and relaxation effects are strongly affected by inversion of the type of substrate-induced strain, but remain essentially unchanged by varying the individual layer thicknesses. In our study, we show that, on the contrary, the transport and magnetic properties of the SLs are almost unaffected by inversion of the type of substrate-induced strain, but qualitatively transformed by varying the number of consecutive unit cells within the LaNiO_3 layers. Since the metal-insulator and spin-ordering transitions occur in the $N = 2$ SLs irrespective of whether the substrate-induced strain is compressive or tensile, strain-induced local structural distortions and interfacial defects are ruled out as primary driving forces.

Figure 1 of the main text shows contour maps of the diffracted X-ray intensity distribution in the vicinity of the 103 perovskite Bragg peak for three representative samples: $N = 4$ and $N = 2$ SLs grown on LaSrAlO_4 (001), and an $N = 2$ SL on SrTiO_3 (001). The analysis of the averaged in-plane and out-of-plane lattice constants (Table SI) indicates that com-

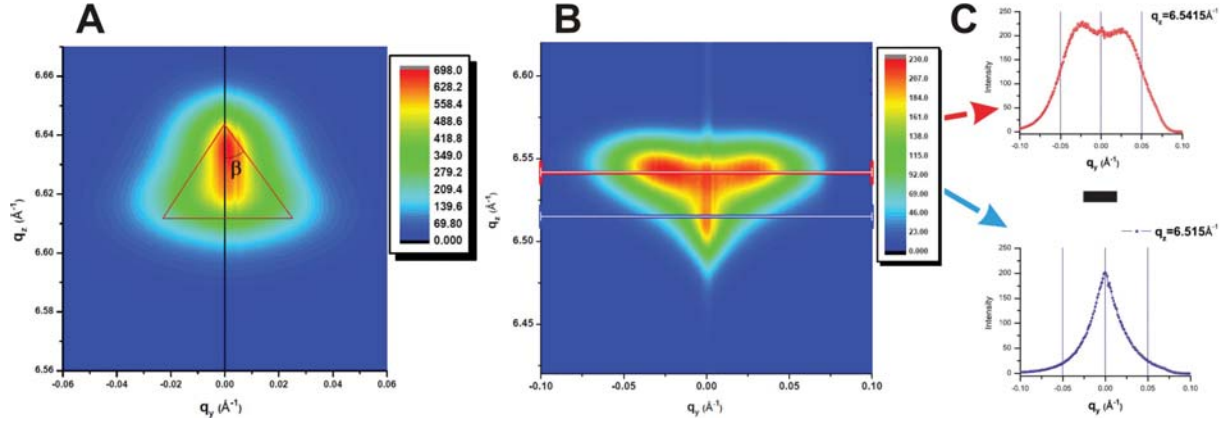


Figure S4: Reciprocal-space maps in the vicinity of the symmetric (004) peak of the 100 nm thick $N = 2$ superlattices on (A) SrTiO₃ and (B) LaSrAlO₄ substrates. The relaxation triangle is highlighted with a red line in (A). The angle $\beta \approx 2^\circ$ quantifies the amount of gradual relaxation the SL has. (C) Horizontal cuts along the indicated in (B) q_z values. The separation of the two twin peaks reveal the formation of twin domains.

pressive strain reduces the in-plane lattice parameter by $\Delta a/a \approx 1.8\%$ relative to the bulk LaNiO₃ lattice, whereas tensile strain results in a reduction of the out-of-plane lattice constant by $\Delta c/c \approx 1.2\%$. These two types of local distortions in the perovskite structure are accommodated by rotations of the NiO₆ octahedra about different Cartesian axes (S7), which, in turn, exert an inequivalent influence on the LaNiO₃ electronic structure. A distribution of the diffracted intensity near the epilayer reflection for SLs grown on LaSrAlO₄ has a characteristic triangular shape, with dispersion along the in-plane (Q_x) direction towards the 103 Bragg reflection of strain-free bulk LaNiO₃. This is in contrast to the tensile-strained SLs grown on SrTiO₃, where the strain relaxation is characterized by nearly elliptical contour lines close to the 103 Bragg reflection of cubic LaAlO₃. The tensile strain of SrTiO₃ is $(67 \pm 3)\%$ relaxed, and by comparing with SLs of less total thickness, we identified a faint gradient-profile-relaxation effect as function of overlayer thickness, similar to the behavior observed in semiconductor heterostructures (S8, S9). In addition to Fig. 1 of the main text, Fig. S4 shows RSMs of the symmetric 004 perovskite Bragg peak measured with synchrotron radiation at the MPI-MF beamline of the ANKA facility at the Karlsruhe Institute of Technology. The diffracted x-ray intensity distribution for

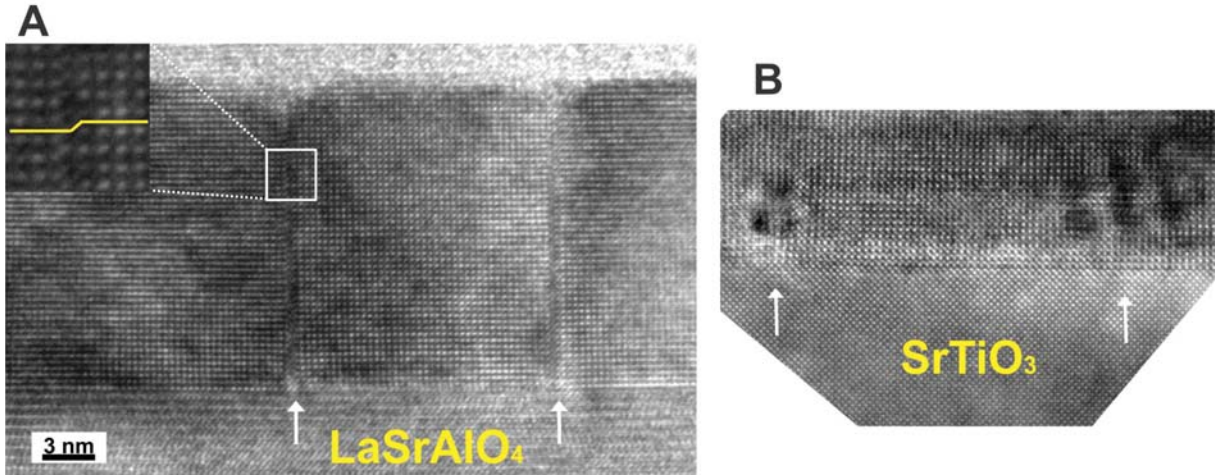


Figure S5: High-resolution TEM micrographs of $\text{LaAlO}_3|\text{LaNiO}_3$ SLs on (A) LaSrAlO_4 and (B) SrTiO_3 substrates. Defects are marked by arrows. The inset in (A) shows a magnified area close to a planar defect.

the $N = 2$ SL on SrTiO_3 (Fig. S4A) exhibits the triangular shape described in Refs. S8 and S9. The effect of triangular relaxation was not observed in the thinner SL (not shown). Because the lattice constants of the thin SL are almost equal to the ones of the thick sample, the SLs grown on SrTiO_3 seem to relax abruptly at the beginning of the growth. Further, from the peak shape evolution, the SL gradually relaxes the tensile strain. The subtle thickness evolution of the layer's relaxation indicates that it is the substrate surface where abrupt strain-adapting mechanisms take place. The effect of tensile strain on TMO heterostructures may produce oxygen vacancies (S10), which give rise to a different valence state of the Ni ion at the substrate interface (S1). Figures S4B and S4C show that the distribution of the diffracted intensity near the epilayer reflection for SLs grown on LaSrAlO_4 has a double-peak splitting along the in-plane (Q_x) direction. This intensity pattern (only seen in thicker SLs grown on LaSrAlO_4) suggests the formation of twinning domains, as described in Refs. S11, S12. The two different relaxation mechanisms in the perovskite structure are confirmed by TEM measurements performed on samples grown under the same conditions as in our study. Figure S5 shows high-resolution TEM micrographs (recorded by a JEOL JEM4000FX microscope) of the $\text{LaNiO}_3 - \text{LaAlO}_3$

layer systems. In the case of the LaSrAlO_4 substrate (Fig. S5A) planar defects are visible (marked by arrows) which are oriented perpendicular to the substrate plane and extend through the entire SL. As shown in the magnified inset image, the stacking sequence changes at these faults (yellow broken line). The size of the defect-free blocks varies between 15 and 50 nm. The microstructure of the layer system on the SrTiO_3 substrate (Fig. S5B) only very occasionally shows planar defects. Instead, localized defects are found close to the substrate (marked by arrows). These defects can be associated with the creation of oxygen vacancies and changes in the oxygen coordination of Ni ions at the substrate interface. Recent photon energy-dependent hard x-ray photoelectron spectroscopy measurements on some of our samples have confirmed that the initial growth on the SrTiO_3 surface leads to the Ni^{2+} valence state (S13). The oxygen vacancy formation energy gradually decreases with increasing the in-plane perovskite lattice spacing (S14), which can explain the marked difference in the oxygen vacancy concentration in thin films grown under tensile or compressive strain (S10). Nevertheless, in our study, the temperature-induced phase transitions occur in the $N = 2$ (but not in $N = 4$) SLs irrespective of whether the substrate-induced strain is compressive or tensile, which clearly distinguishes these transitions from those in highly oxygen deficient $\text{LaNiO}_{3-\delta}$ ($\delta \geq 0.25$) (S15, S16). Moreover, the reduced insulating phases require more than 1/3 of divalent Ni^{2+} in square planar (vs. perovskite octahedral) sites. Based on the detailed characterization of our samples by means of XRD, XAS, RSM, HAXPES, and TEM we can definitively rule out such a scenario.

In conclusion, our analysis confirms the excellent quality of the synthesized SLs, which exhibit abrupt interfaces and excellent crystallinity. Defect-free, atomically precise 15-50 nm blocks are separated by ~ 1 u.c. stacking faults. These planar defects are inevitably caused by strain relaxation effects, and can block the current flow through the atomically thin layers. We have therefore used advanced local probes, such as spectroscopic ellipsometry and low-energy muons, to study the intrinsic electronic transport and magnetic properties of the heterostructures.

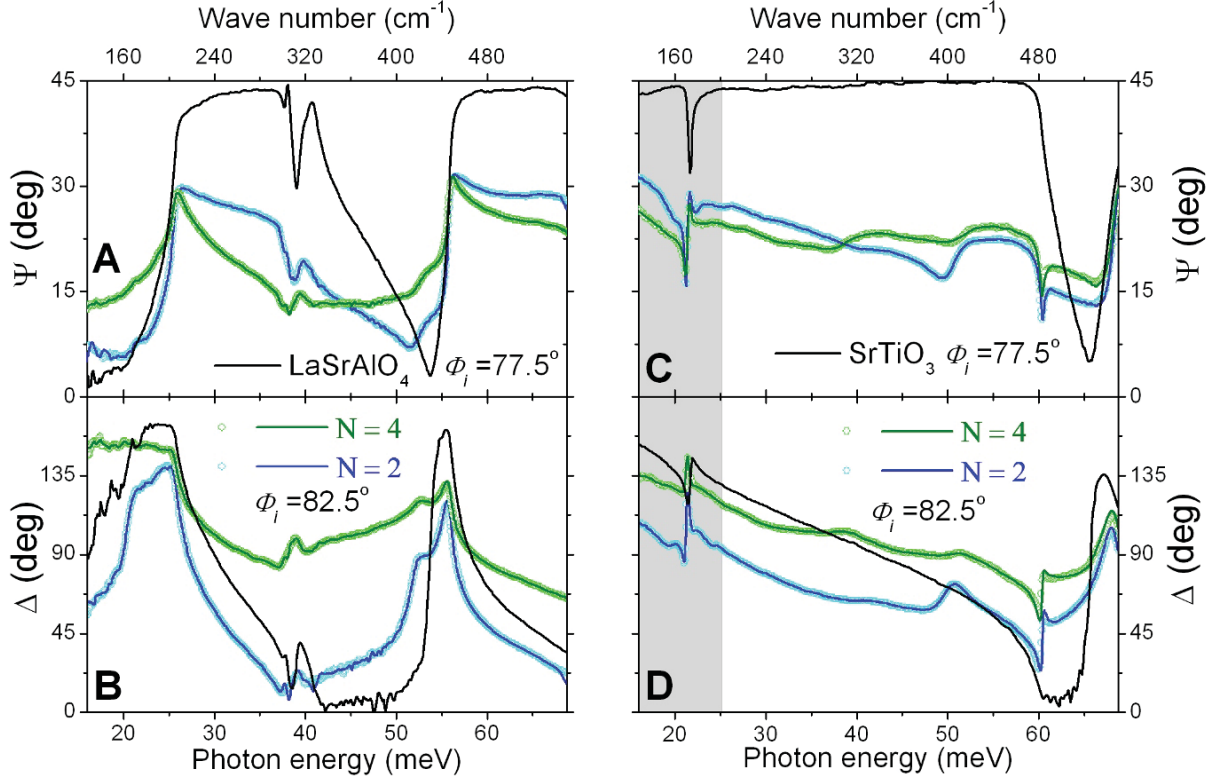


Figure S6: Experimental (open circles) and best-fit calculated (solid lines) ellipsometry spectra of the $N = 2$ and $N = 4$ SLs on (A,B) LaSrAlO_4 at $T = 175$ K and (C,D) SrTiO_3 at $T = 100$ K. The angle of incidence of the polarized light was $\Phi_i = 82.5^\circ$. Ellipsometry spectra of the bare substrates measured at $\Phi_i = 77.5^\circ$ are shown for comparison (black solid lines). The gray shaded area in (C,D) indicates the region where the data analysis is affected by dielectric microwave dispersion of the ferroelectric soft mode of SrTiO_3 .

Spectroscopic ellipsometry measurements and data analysis

We have used wide-band spectroscopic ellipsometry to accurately determine the dynamical electrical conductivity and permittivity of the SLs. The distinct advantages of ellipsometry are as follows. (i) In contrast to dc transport experiments, this method exposes the intrinsic electrodynamic response of the SLs, which is not influenced by the substrate, contacts, and extended defects. (ii) As a low-energy spectroscopic tool, it serves to determine critical parameters of the metal-insulator transition such as the energy gap and the density of carriers localized below T_{MI} . (iii) In comparison with other spectroscopic techniques, ellipsometry yields the

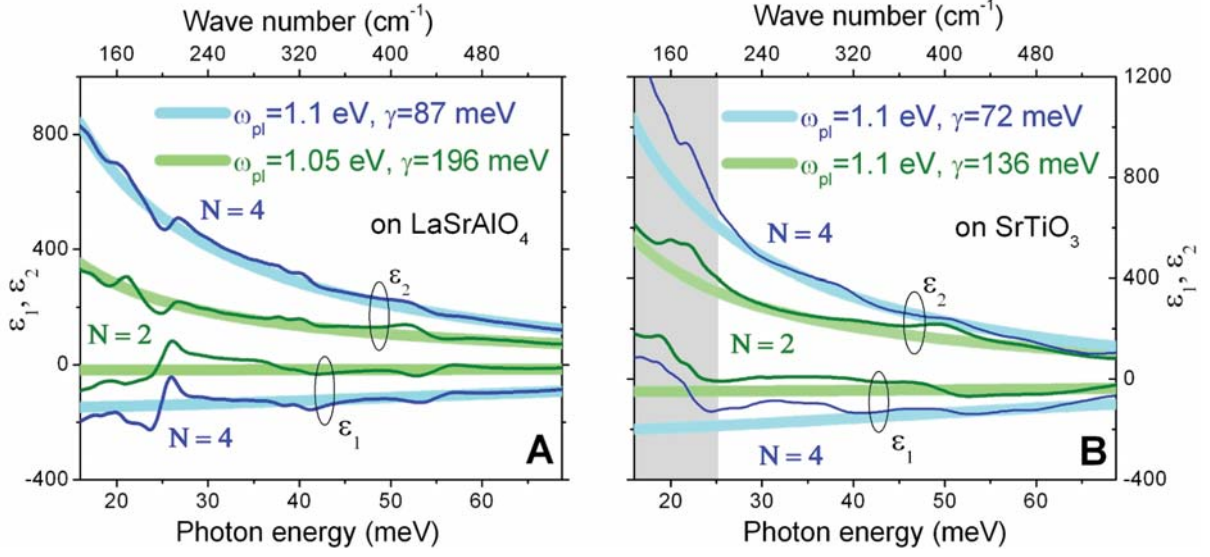


Figure S7: Best-fit model functions $\epsilon_1(\omega)$ and $\epsilon_2(\omega)$ for the $N = 2$ and $N = 4$ SLs on (A) LaSrAlO_4 at $T = 175$ K and (B) SrTiO_3 at $T = 100$ K, as obtained by inversion of the ellipsometric parameters in Fig. S6. The shaded lines represent the Drude model simultaneous fit to both $\epsilon_1(\omega)$ and $\epsilon_2(\omega)$ with parameters ω_{pl} and γ described in the legends. The gray shaded area in (B) indicates the region where the model fitting curves deviate significantly from the data.

frequency-dependent complex dielectric function without the need for reference measurements and Kramers-Kronig transformations. (iv) Variable angle ellipsometry is very sensitive to thin-film properties due to the oblique incidence of light, and it is generally used to derive optical constants of thin films and complex heterostructures (S17).

The experimental setup comprises three ellipsometers to cover the spectral range of 12 meV to 6.5 eV. For the range 12 meV to 1 eV, we used a home-built ellipsometer attached to a standard Fast-Fourier-Transform Bruker 66v/S FTIR interferometer. The far-infrared measurements were performed at the infrared beamline IR1 of the Angstrm Quelle Karlsruhe ANKA synchrotron light source at the Karlsruhe Institute of Technology. For the mid-infrared measurements, we used the conventional glow-bar light source from a Bruker 66v/S FTIR. Finally, temperature dependencies of the pseudo-dielectric permittivity ϵ_1^* at $\hbar\omega = 0.8$ eV were measured with a Woollam variable angle spectroscopic ellipsometer (VASE) equipped with an ultra

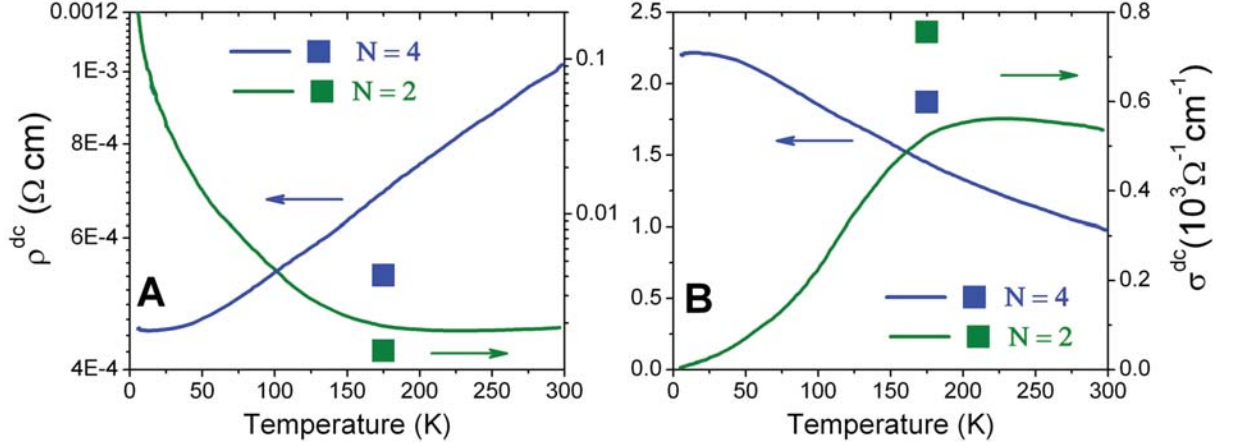


Figure S8: Temperature dependence of the *dc* (A) resistivity and (B) conductivity of the $N = 2$ (green) and $N = 4$ (blue) SLs on LaSrAlO_4 . Solid squares represent the conductivity obtained from the Drude model parameters in the legend of Fig. S7A, which exceeds the corresponding σ^{dc} ($T = 175$ K) values by less than 20 %.

high-vacuum cold-finger cryostat operated at $< 5 \times 10^{-9}$ mbar chamber pressure.

The inherent capacity of Woollam VASE ellipsometers to measure relative changes of the dielectric function on the order of 10^{-2} was boosted to an unprecedented level of 10^{-4} using temperature-modulation measurements of the dielectric constant at particular photon energies. The ellipsometric angles Ψ and Δ are defined through the complex Fresnel reflection coefficients for light polarized parallel (r_p) and perpendicular (r_s) to the plane of incidence, $\tan \Psi e^{i\Delta} = r_p/r_s$. Figure S6 shows representative infrared spectra of $\Psi(\omega)$ and $\Delta(\omega)$ for the $N = 4$ and 2 SLs and for the bare LaSrAlO_4 and SrTiO_3 substrates. The details of the data analysis have been discussed elsewhere (S18). The SLs were treated as single-layer films according to an effective-medium approximation with a mixture of the nickelate and aluminate layers. A wavelength-by-wavelength regression procedure has been employed to extract the real and imaginary parts of the dielectric function (S19). Figure S7 shows the best-fit model functions $\varepsilon_1(\omega)$ and $\varepsilon_2(\omega)$ obtained by inversion of the ellipsometric parameters in Fig. S6. The infrared spectra are well described by a broad Drude response $\varepsilon(\omega) = \varepsilon_\infty - \omega_{pl}^2/(\omega^2 + i\omega\gamma)$ with a ratio of scattering rate and plasma frequency $\gamma/\omega_{pl} \approx 0.1 - 0.2$ that is typical for bulk

complex oxides. The parameters in the Drude fit are well constrained, because both $\varepsilon_1(\omega)$ and $\varepsilon_2(\omega)$ are available. The deviation of the Drude fit from the measured $\varepsilon_1(\omega)$ and $\varepsilon_2(\omega)$ below 30 meV in Fig. S7B (gray shadow area) can reflect the uncertainty in the inversion procedure for SLs on SrTiO₃ due to the microwave dispersion of the ferroelectric soft mode of SrTiO₃ (S20) and/or due to the presence of a dead layer with reduced conductivity at the substrate interface (Fig. S5B). This low-energy uncertainty does not, however, affect the relative spectral weight reduction, $\Delta SW \approx 0.03$ ($\pm 10\%$) per Ni atom within the gap energy range below $\Omega_G \approx 0.43$ eV, at the metal insulator transition in the $N = 2$ SL on SrTiO₃.

The effective mass enhancement m^*/m is estimated from the plasma frequency as

$$m^*/m = \frac{4\pi e^2 n}{m\omega_{pl}^2} \approx \frac{11.7}{(\omega_{pl}, [eV])^2}, \quad (1)$$

where $n = \frac{1}{2} \times 1.7 \times 10^{22} \text{ cm}^{-3}$, by assuming one electron per Ni atom. We note that ω_{pl} is almost independent of N , implying the volume fraction of the metallic LaNiO₃ layers remains the same in all SLs. With $\omega_{pl} \approx 1.1$ eV, as derived from the Drude model fit in Fig. 2A, we obtain $m^*/m \approx 10$ which is in good agreement with the value for bulk LaNiO₃ from the specific heat measurements (S21). Using the Fermi energy $E_F = 0.5$ eV derived from the thermopower of LaNiO₃ (S21), we estimate the Fermi velocity as

$$v_F = c\sqrt{\frac{2E_F}{mc^2} \frac{m}{m^*}} \approx 1.33 \times 10^7 \text{ cm/s}. \quad (2)$$

The mean free path, l , can be estimated from

$$l [\text{\AA}] = v_F \tau = \frac{v_F}{2\pi c \gamma} = 6.57 \times 10^{-5} \frac{v_F [\text{cm/s}]}{\gamma [\text{meV}]} \approx \frac{874}{\gamma [\text{meV}]}. \quad (3)$$

With $\gamma \approx 200$ meV (90 meV), as derived from the Drude model fit in Fig. 2A and Fig. S7A, we obtain $l = 4.4$ \AA (9.7 \AA) for the $N = 2$ ($N = 4$) SL on LaSrAlO₄. For the $N = 2$ ($N = 4$) SL on SrTiO₃ we estimate $l = 6.4$ \AA (12 \AA), respectively. Remarkably, the mean free path correlates with the individual LaNiO₃ layer thickness, testifying, along with the constant volume fraction of the metallic layers, to the atomic quality of the interfaces .

Our results indicate that, even in the $N = 2$ samples at $T \gtrsim T_{MI}$, the conductivity of the LaNiO_3 layers exhibits a clearly metallic temperature and frequency dependence. We define T_{MI} as the temperature at which the temperature derivatives of both $\varepsilon_2(T)$ (Figs. 2A and 2B) and $\varepsilon_1(T)$ (Figs. 2C and 2D) change sign. The consistent temperature evolution of ε_1 and ε_2 over a broad range of photon energies demonstrates the intrinsic nature of the charge-localization transition observed in SLs with $N = 2$. In the $\omega \rightarrow 0$ limit this criterion is analogous to a sign change of the temperature derivative of the dc resistivity, $d\rho/dT$, observed at T_{MI} in bulk $R\text{NiO}_3$. This is in contrast to results of recent dc electrical resistivity measurements where the insulating behavior of 2 u.c. thick LaNiO_3 is attributed to variable range hopping transport (S22) or film-substrate interface effects (S23, S24). For a thickness of $N = 2$ u.c. the behavior of $(\text{LaNiO}_3)_N/(\text{SrMnO}_3)_2$ SLs is insulating over the entire temperature range, whereas the $N = 4$ u.c. SL is metallic with an upturn in resistivity below 50 K. Even in the $N = 4$ u.c. metallic sample, the mean free path l is estimated to be less than a single unit cell (S22). This suggests that Anderson localization induced by disorder is responsible for the insulating behavior in these systems, in contrast to the sharp temperature dependence observed in our SLs that indicates a metal-insulator transition driven by collective interactions. Ultrathin single films of LaNiO_3 show a crossover from metallic to insulating behavior at a larger thickness (S23, S24), which varies from 6 u.c. to 13 u.c. depending on the substrate. We argue that the presence of planar stacking fault defects and a dead layer with reduced conductivity at the substrate interface, as discussed above (Fig. S5), makes the analysis of the temperature-dependent resistivity measurements challenging and inconclusive about the conduction mechanism of ultrathin LaNiO_3 films. Nevertheless, in order to directly compare our results with those reported in Refs. S22, S23, and S24, we have also performed dc resistivity measurements on the $N = 2$ and $N = 4$ SLs on LaSrAlO_4 . Figure S8 shows that the dc resistivity of the $N = 2$ SL exhibits a crossover from metallic to insulating phase behavior below $T_{MI} \approx 150$ K. The sharp temperature dependence in the insulating state does not fit to the stretched exponential function (S22) and can not be attributed to variable range hopping

transport. Figure S8 also shows that our *dc* and optical conductivity data (Figs. 2A and S7A) are in close agreement. This resemblance once more indicates a low density of stacking faults in our samples.

Low-energy μ SR instrumentation and data analysis

Low energy muon spin rotation/relaxation (LE- μ SR) uses $\sim 100\%$ spin polarized positive muons of tunable keV-scale energy to study local magnetic properties of thin films or heterostructures as a function of the muon implantation depth. The details of the data acquisition and analysis have been described elsewhere (S25, S26). More details of the LE- μ SR methods and apparatus can be found on the website of the LEM group at Paul Scherrer Institute (S27). This technique has been recently successfully applied to the case of magnetic ultra-thin films (S28) and wires (S29). Figure S9 shows the muon stopping profile calculated for

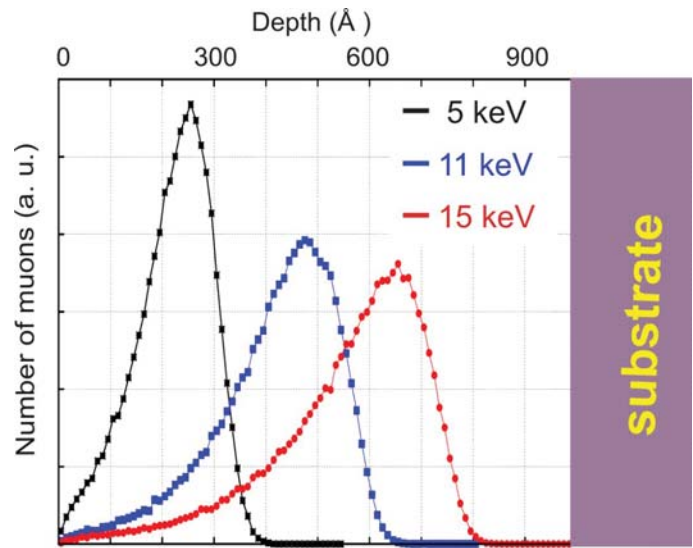


Figure S9: Muon stopping profile in the $N = 2$ SL showing the calculated probability that μ^+ with an implantation energy of 5 keV (black), 11 keV (blue), and 15 keV (red) comes to rest at a certain depth near the surface.

$\text{LaAlO}_3|\text{LaNiO}_3$ SLs using the Monte Carlo algorithm TRIM.SP (S30, S31).

In our study we found that varying the stopping distribution of μ^+ on the scale of about 50-800 Å through the control of the implantation energy between 5-15 keV had no effect on the μ SR spectra. The experimental LE- μ SR curves in Figs. 3A to 3D were measured with muons of energy 10 keV, which are implanted at a mean depth of 45 nm. The initial asymmetry,

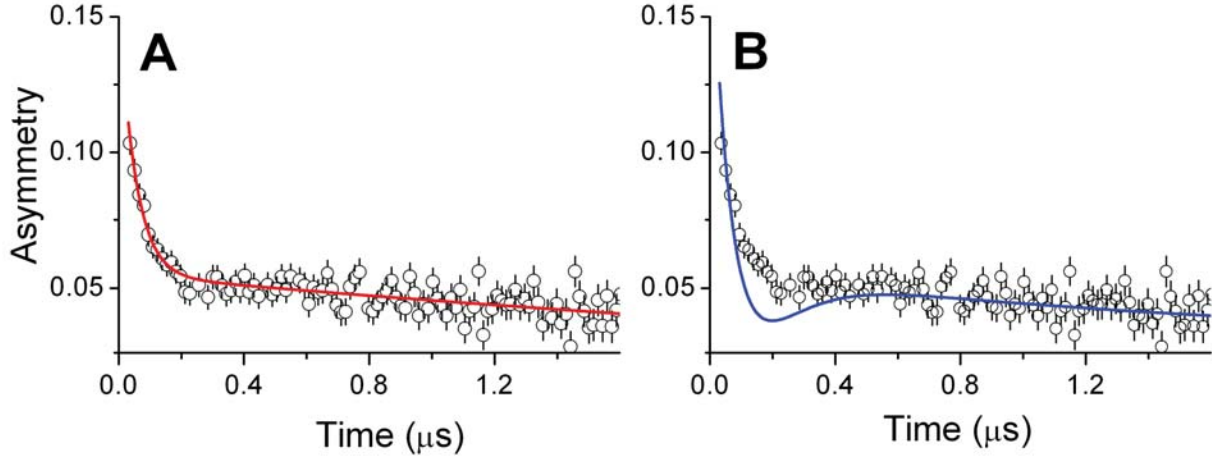


Figure S10: Zero-field μ SR function observed in the $N = 2$ SL on LaSrAlO_4 at 5 K. The solid lines represent the best-fit curves for (A) the two-component model function described in the manuscript and (B) Eq.(4), respectively.

$A(0) \approx 0.18$, is smaller than the asymmetry of the LE- μ SR setup of ≈ 0.27 , because only $2/3$ of the muon beam with a diameter of about 2 cm hit the sample with an area of $1 \times 2 \text{ cm}^2$. The sample was surrounded by a Ni-coated sample holder, which causes a very fast depolarization ($< 0.06 \mu\text{s}$) of muons missing the sample.

The obtained spectra μ SR spectra yield the probability distribution of the local magnetic field at the muon sites. As a local probe, μ SR does not allow definite conclusions about the magnetic ordering pattern in the $N = 2$ SLs. However, we rule out ferromagnetism based on an estimate of the ordered moment on the Ni sites from the μ SR lineshape, $\mu_{\text{Ni}} \gtrsim 0.5\mu_B$ (see the main text of the manuscript). If these moment were co-aligned in the ordered state, the corresponding total moment $M = \mu_{\text{Ni}}n_{\text{Ni}}V_{\text{SL}} \gtrsim 7.7 \times 10^{-4} \text{ emu}$ would have been readily detected in magnetization measurements. The absence of such an effect, which we confirmed in magnetometric measurements with sensitivity $\sim 10^{-7} \text{ emu}$.

We can also rule out a spin-glass state as the ground state of $N = 2$ SLs, bearing in mind that oxygen deficient $\text{LaNiO}_{2.75}$ exhibits spin-glass like behavior at low temperatures (S15). A spin-glass state develops gradually due to randomly fluctuating local moments. In this case, the spin relaxation function should be exponential with a unique rate already at temperatures

above about four times the actual glass transition temperature, $\sim 80 - 100$ K (S32), which is at variance with the sharp temperature onset of the local moment observed in our data (Fig. 3A and solid squares in Fig. 4 of the manuscript). A similarly sharp transition was very recently observed by x-ray magnetic circular dichroism (XMCD) measurements in a magnetic field of 5T on a sample with $N = 2$ grown under the same conditions (S33).

Additional evidence against a spin glass state can be derived from an analysis of the muon relaxation function. At low temperature, the spin-glass relaxation function in zero field can be described by (S34)

$$A(t) = A_0 \left[\frac{1}{3} \exp(-\sqrt{\lambda_d t}) + \frac{2}{3} \left(1 - \frac{\sigma^2 t^2}{\sqrt{\lambda_d t + \sigma^2 t^2}} \right) \exp(-\sqrt{\lambda_d t + \sigma^2 t^2}) \right] \quad (4)$$

with $\sigma \equiv \sqrt{q} \sigma_s$ and $\lambda_d \equiv 4\sigma_s^2(1 - q)/\nu$, where q is the Edwards-Anderson order parameter with the purely static and dynamic limits, $q = 1$ and $q = 0$, respectively, σ_s is the static width of local fields at the muon site, and ν is the rate of the randomly fluctuating moments. This form of the relaxation function is expected for μ^+ in coexisting static and dynamic random local fields. The fit of Eq. (4) to the time evolution of the zero-field muon spin polarization for the $N = 2$ SL on LaSrAlO₄ at 5 K (Fig. S10) gives reasonable parameters, i.e. close to the static limit with $q \approx 0.993$, $\sigma_s = 11 - 15 \mu\text{s}^{-1}$, and $\nu \approx 2 \mu\text{s}^{-1}$. Nevertheless, the simpler two-component model function, as described in the manuscript, provides a better fit to the data below $0.2 \mu\text{s}$ than the spin-glass function of Eq. (2). The analysis is consistent with long-range static antiferromagnetic order and confirms the conclusion of our manuscript.

References and Notes

- [S1] J. Liu *et al.*, *Appl. Phys. Lett.* **96**, 133111 (2010).
- [S2] S. Macke, S. Brück, and E. Goering, *ReMagX x-ray magnetic reflectivity tool* (<http://www.mf.mpg.de/remagx.html>).
- [S3] L. G. Parratt, *Phys. Rev.* **95**, 359 (1954).

- [S4] C. T. Chantler, *J. Phys. Chem. Ref. Data* **29**(4), 597 (2000).
- [S5] E. Benckiser *et al.*, *Nature Mat.* **10**, 189 (2011).
- [S6] A. Frano, *MSc Thesis*, University of Stuttgart (2010).
- [S7] S. J. May *et al.*, *Phys. Rev. B* **82**, 0141108 (2010).
- [S8] H. Heinke *et al.*, *J. Crystal Growth* **135**, 41 (1994).
- [S9] H. Heinke *et al.*, *J. Phys. D: Appl. Phys.* **28**, A104 (1995).
- [S10] F. Conchon *et al.*, *Appl. Phys. Lett.* **91**, 192110 (2007).
- [S11] U. Gebhardt *et al.*, *Phys. Rev. Lett* **98**, 096101 (2007).
- [S12] U. Gebhardt, *PhD Thesis*, University of Stuttgart (2006).
- [S13] P. Helmecke and R. Claessen, *private communication*.
- [S14] Yu. F. Zhukovskii *et al.*, *Solid State Commun.* **149**, 1359 (2009).
- [S15] R. D. Sanchez *et al.*, *Phys. Rev. B* **54**, 16574 (1996).
- [S16] M. Kawai *et al.*, *Appl. Phys. Lett.* **94**, 082102 (2009).
- [S17] H. G. Tompkins, E. A. Irene, *Handbook of Ellipsometry* (Springer, Germany, 2005).
- [S18] J. W. Freeland *et al.*, *Phys. Rev. B* **81**, 094414 (2010).
- [S19] J. A. Woollam Co., Inc., *WVASE32 Spectroscopic Ellipsometry Data Acquisition and Analysis Software* (<http://www.jawoollam.com>); A. V. Tikhonravov and M. K. Trubetskoy, *Optilayer Thin Film Software* (<http://www.optilayer.com>).
- [S20] A. A. Sirenko *et al.*, *Nature* **404**, 373 (2000).
- [S21] X. Q. Xu *et al.*, *Phys. Rev. B* **48**, 1112 (1993).

- [S22] S. J. May, T. S. Santos, and A. Bhattacharya, *Phys. Rev. B* **79**, 115127 (2009).
- [S23] R. Scherwitzl *et al.*, *Appl. Phys. Lett.* **95**, 222114 (2009).
- [S24] J. Son *et al.*, *Appl. Phys. Lett.* **96**, 062114 (2010).
- [S25] T. Prokscha *et al.*, *Nucl. Instr. Meth. A* **595**, 317 (2008).
- [S26] For conventional μ SR methods see, for example, J.E. Sonier, *μ SR brochure* (<http://musr.org/intro/musr/muSRBrochure.pdf>).
- [S27] Web site of the LEM group at PSI: <http://lmu.web.psi.ch/lem/index.html>.
- [S28] S. R. Dunsiger *et al.*, *Nature Mater.* **9**, 299 (2010).
- [S29] M. Shay *et al.*, *Phys. Rev. B* **80**, 144511 (2010).
- [S30] E. Morenzoni *et al.*, *Nucl. Instrum. Methods Phys. Res. B* **192**, 254 (2002).
- [S31] W. Eckstein, *Computer Simulation of Ion-Solid Interactions* (Springer, Berlin, 1991).
- [S32] I. A. Campbell *et al.*, *Phys. Rev. Lett.* **72**, 1291 (1994).
- [S33] M. Wu, E. Benckiser, and E. Goering, *private communication*.
- [S34] Y. J. Uemura *et al.*, *Phys. Rev. B* **31**, 546 (1985).